Micromechanics of brittle creep in rocks

N. Brantut,[1] P. Baud,[2] M. J. Heap,[2] and P. G. Meredith[1]

Received 8 March 2012; revised 13 June 2012; accepted 13 June 2012; published 25 August 2012.

[1] In the upper crust, the chemical influence of pore water promotes time dependent brittle deformation through sub-critical crack growth. Sub-critical crack growth allows rocks to deform and fail at stresses well below their short-term failure strength, and even at constant applied stress ("brittle creep"). Here we provide a micromechanical model describing time dependent brittle creep of water-saturated rocks under triaxial stress conditions. Macroscopic brittle creep is modeled on the basis of microcrack extension under compressive stresses due to sub-critical crack growth. The incremental strains due to the growth of cracks in compression are derived from the sliding wing crack model of *Ashby and Sammis* (1990), and the crack length evolution is computed from Charles' law. The macroscopic strains and strain rates computed from the model are non linear, and compare well with experimental results obtained on granite, low porosity sandstone and basalt rock samples. Primary creep (decelerating strain) corresponds to decelerating crack growth, due to an initial decrease in stress intensity factor with increasing crack length in compression. Tertiary creep (accelerating strain as failure is approached) corresponds to an increase in crack growth rate due to crack interactions. Secondary creep with apparently constant strain rate arises as an inflexion between those two end-member phases. The minimum strain rate at the inflexion point can be estimated analytically as a function of model parameters, effective confining pressure and temperature, which provides an approximate creep law for the process. The creep law is used to infer the long term strain rate as a function of depth in the upper crust due to the action of the applied stresses: in this way, sub-critical cracking reduces the failure stress in a manner equivalent to a decrease in cohesion. We also investigate the competition with pressure solution in porous rocks, and show that the transition from sub-critical cracking to pressure solution dominated creep occurs with increasing depth and decreasing strain rates.

Citation: Brantut, N., P. Baud, M. J. Heap, and P. G. Meredith (2012), Micromechanics of brittle creep in rocks, *J. Geophys. Res.*, *117*, B08412, doi:10.1029/2012JB009299.

1. Introduction

[2] The deformation of rocks in the brittle field (at modest pressures and temperatures, typical of shallow crustal conditions) is predominantly governed by the growth and coalescence of a crack network, and macroscopic brittle failure is characterized by the formation of a fault in the rock mass [e.g., *Scholz*, 2002; *Paterson and Wong*, 2005]. In a chemically inert environment, the growth of cracks is well described by linear elastic fracture mechanics, and the appropriate criterion for crack growth is that the stress intensity factor at the crack tips reaches a critical value, which is an intrinsic material property, known as the fracture toughness. The faulting process is then purely controlled by the stress acting on the rock. Indeed, laboratory rock deformation tests performed at fast strain rates, above 10^{-5} s^{-1}, generally show that brittle deformation is primarily dictated by the applied stress. Based on linear elastic fracture mechanics, micromechanical approaches have been used to predict the mechanical behavior of rocks in compressive regimes, typically by modeling the growth of "wing" cracks from preexisting defects [e.g., *Kachanov*, 1982a, 1982b; *Nemat-Nasser and Horii*, 1982; *Costin*, 1985; *Ashby and Sammis*, 1990].

[3] However, laboratory experiments demonstrate that rocks experience some creep and fail by static fatigue at stresses significantly below their short term failure strength [e.g., *Kranz*, 1979; *Carter et al.*, 1981; *Kranz et al.*, 1982; *Baud and Meredith*, 1997; *Heap et al.*, 2009a, 2011]. This time dependent brittle process, hereafter referred to as brittle creep, is explained by slow crack growth when the stress intensity factor at crack tips is lower than the fracture

[1]Rock and Ice Physics Laboratory, Department of Earth Sciences, University College London, London, UK.
[2]Laboratoire de Géophysique Expérimentale, Institut de Physique de Globe de Strasbourg, UMR 7516 CNRS, Université de Strasbourg/EOST, Strasbourg, France.

Corresponding author: N. Brantut, Rock and Ice Physics Laboratory, Department of Earth Science, University College London, Gower Street, London WC1E 6BT, UK. (nicolas.brantut@normalesup.org)

0148-0227/12/2012JB009299

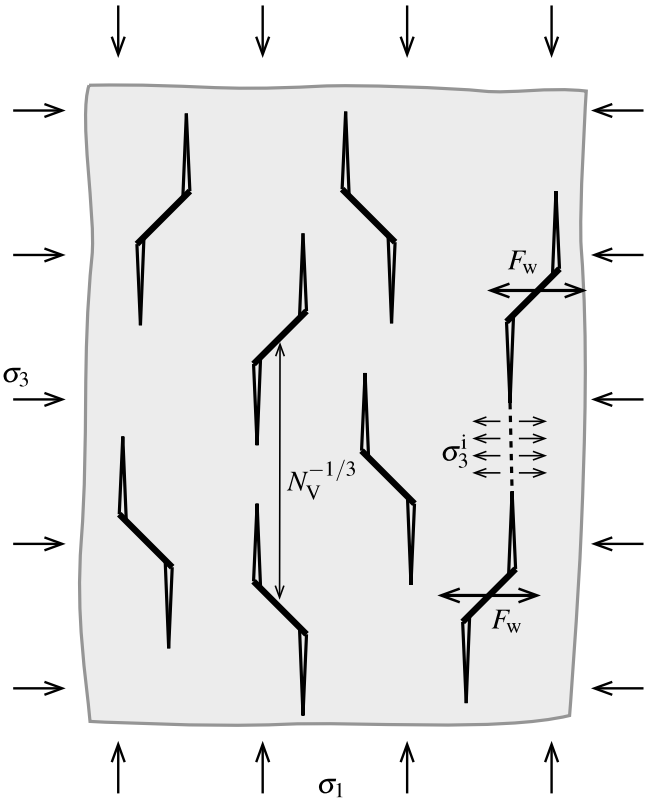

Figure 1. Schematic of the problem set up (modified from *Ashby and Sammis* [1990]).

toughness, i.e., sub-critical crack growth [e.g., *Atkinson*, 1984]. The main underlying physical mechanism of sub-critical crack growth under upper crustal conditions is stress corrosion, where the amplified stresses at crack tips preferentially activate chemical reactions with strained crack tip bonds, such as the hydrolysis of silicon-oxygen bonds in the quartz-water system [e.g., *Michalske and Freiman*, 1982]. Theoretical and experimental studies [e.g. *Wan et al.*, 1990] have shown that a lower stress limit to stress corrosion exists, which in turn affects the lower stress limit to rock fracture in brittle creep conditions.

[4] Several micromechanical approaches have been proposed to model the macroscopic behavior of rocks in the brittle creep regime, based on the inclusion of the stress corrosion effect within conventional fracture mechanics models. Analytical solutions for the macroscopic strain induced by the growth of a single crack have been determined by *Kachanov* [1982c] and *Kemeny* [1991]. *Lockner* [1993] calculated approximate solutions for the volumetric strain induced by the growth of a crack population without interactions. *Yoshida and Horii* [1992] developed a micromechanical model for brittle creep with a simplified failure criterion and no explicit formulation for crack interactions. Creep arising from sub-critical crack growth with crack interactions has been modeled by *Costin* [1985] using a collinear array of cracks. Among the studies mentioned above, none systematically explores the parameter space, for instance the effect of confining pressure or temperature on creep strain rates, or the effect of preexisting defect density or initial crack length. In addition, the link between the short term failure strength and the brittle creep conditions remains to be explored in a single micromechanical framework. The recent experimental dataset obtained by *Heap et al.* [2009a, 2009b, 2011], exploring the effects of pressure, stress and temperature on creep strain rates in various rock types, provides the opportunity to test the validity of models and to refine plausible ranges for model parameters.

[5] Here we present an extension of the classical micromechanical model of *Ashby and Sammis* [1990] to account for sub-critical crack growth. In the *Ashby and Sammis* [1990] formulation, microcrack interactions are taken into account (in a global sense; see below for details), and the model is able to predict reasonably well the short term failure strength of compact rocks at low confining pressures (typically below 100 MPa, see *Bhat et al.* [2011]). We first present the model formulation, including sub-critical crack growth by stress corrosion, and give the governing differential equation for macroscopic strain rate during brittle creep. Due to the complexity of the model, analytical solutions are unfortunately not tractable and only an incremental strain-crack length relation can be determined. The basic features of the model are then presented and the parameter space is explored to determine the influence of confining pressure, stress and initial damage on the brittle creep strain rates. Finally, the model outcomes are discussed in the light of recent experimental data on basalt and sandstone [*Heap et al.*, 2009a, 2011] as well as previously unpublished brittle creep data on Westerly granite.

2. Model Description

2.1. Stress Intensity Factor

[6] In this section, we summarize the assumptions and results given by *Ashby and Sammis* [1990] to determine the stress intensity factor at crack tips in compressive stress states, including crack interactions, in the 3D case. Let us consider an isotropic elastic solid that contains an initial set of penny shaped microcracks of radius a, and all aligned at an angle Ψ to the maximum principal stress σ_1 (Figures 1 and 2). As noted by *Bhat et al.* [2011], this assumption means that the brittle behavior of the rock is driven by the nucleation and propagation of a dominant set of

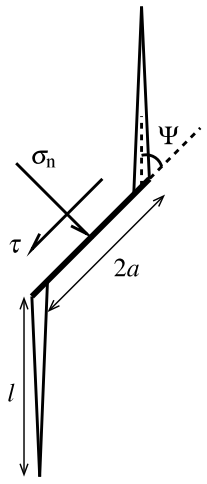

Figure 2. Wing crack geometry.

microcracks. In the following we assume $\Psi = \pi/4$, which implies that the dominant microcracks are those subjected to the maximum shear stress. In order to simulate the stress state in a conventional triaxial experiment, we assume that the minimum (σ_3) and the intermediate (σ_2) principal stresses are equal. Stresses are taken positive in compression. In such a geometry, the initial crack density is characterized by a scalar parameter

$$\rho_0 = \frac{4}{3}\pi N_V (\alpha a)^3, \tag{1}$$

where N_V is the number of microcracks per unit volume of the rock, and $\alpha = \cos\Psi$ is the projection of the crack radius in the vertical plane. Throughout this manuscript, the scalar parameter ρ_0 will be referred to as "the crack density parameter", and not simply the crack density, since it differs from the general definition given for instance by *Sayers and Kachanov* [1995] (see Appendix A).

[7] The remote stress state (σ_1, σ_3) produces a shear stress τ and a normal stress σ_n on the crack planes (Figure 2), given by

$$\tau = \frac{\sigma_1 - \sigma_3}{2}\sin 2\Psi, \tag{2}$$

$$\sigma_n = \frac{\sigma_1 + \sigma_3}{2} - \frac{\sigma_1 - \sigma_3}{2}\cos 2\Psi. \tag{3}$$

[8] Sliding on the initial flaws is controlled by a friction coefficient μ. At low stress, if $|\tau| \le \mu|\sigma_n|$, the cracks do not slide and the rock behaves elastically. When the resolved shear stress τ overcomes the static friction, elastic strain initially allows sliding without further crack extension. Wing cracks (see geometry in Figure 2) then initiate at a critical stress expressed by [*Ashby and Hallam*, 1986]

$$\sigma_{1c} = \frac{\sqrt{1+\mu^2}+\mu}{\sqrt{1+\mu^2}-\mu}\sigma_3 + \frac{\sqrt{3}}{\sqrt{1+\mu^2}-\mu}\cdot\frac{K_{IC}}{\sqrt{\pi a}}, \tag{4}$$

where K_{IC} is the critical mode I stress intensity factor of the material (fracture toughness). Here we are only interested in the behavior at stresses higher than σ_{1c}, where wing cracks are already growing from the tips of the initial flaws. Nevertheless, we will make use of relation (4) to determine model parameters independently from the results of brittle creep experiments.

[9] Following *Ashby and Sammis* [1990], we calculate the mode I stress intensity factor at the tips of the wing cracks by approximating the whole kinked crack configuration by a single tensile crack of radius $l + \alpha a$ being opened by a "wedging force"

$$F_w = (\tau + \mu\sigma_n)\pi a^2 \sin\Psi = (A_1\sigma_1 - A_3\sigma_3)a^2, \tag{5}$$

where A_1 and A_3 are constants given by *Ashby and Sammis* [1990]:

$$A_1 = \pi\sqrt{\frac{\beta}{3}}\left[\sqrt{1+\mu^2}+\mu\right], \tag{6}$$

$$A_3 = A_1\frac{\sqrt{1+\mu^2}+\mu}{\sqrt{1+\mu^2}-\mu}. \tag{7}$$

These constants A_1 and A_2 were determined exactly for the 2D case, and *Ashby and Sammis* [1990] merely assumed they would hold in 3D with some ad hoc fitting of the parameter β, the meaning of which is clarified below.

[10] The force F_w and the compressive stress σ_3 generate a mode I stress intensity factor at the tips of the wing cracks of the form [*Ashby and Sammis*, 1990]

$$K_I = \frac{F_w}{[\pi(l+\beta a)]^{3/2}} - \frac{2}{\pi}(\sigma_3 - \sigma_3^i)\sqrt{\pi l}, \tag{8}$$

where β is used to regularize the solution at small l. For our purpose here, the parameter β can be fitted from short term failure tests (for instance from the stress at the onset of cracking), and that value will be used for the brittle creep simulations. Thus, β will not be adjusted to experimental brittle creep data. The second term on the right hand side of relation (8) is the modification of K_I due both to the application of a confining pressure σ_3 and to the interaction between cracks (in the form of an internal stress σ_3^i). Crack interaction is dealt with in a global sense by considering that the wedging force across a vertical section is balanced by an internal stress

$$\sigma_3^i = \frac{F_w}{S - \pi(l+\alpha a)^2}, \tag{9}$$

where $S = \pi^{1/3}(3/(4N_V))^{2/3}$ is the average area associated with each crack on a vertical cross section of the array (Figure 1).

[11] In terms of crack length l, the stress intensity factor is thus expressed as

$$\frac{K_I}{\sqrt{\pi a}} = (A_1\sigma_1 - A_3\sigma_3)(c_1 + c_2) - \sigma_3 c_3, \tag{10}$$

where

$$c_1 = \pi^{-2}(l/a + \beta)^{-3/2}, \tag{11}$$

$$c_2 = 2(\pi\alpha)^{-2}(l/a)^{1/2}\Big/\left[\rho_0^{-2/3} - (1 + l/(\alpha a))^2\right], \tag{12}$$

$$c_3 = (2/\pi)(l/a)^{1/2}. \tag{13}$$

Note that the expressions above correct typographical errors in *Ashby and Sammis* [1990, equation 26] (in which a factor β/α was dropped) and *Bhat et al.* [2011, equation 18] (in which c_2 and c_3 were interchanged).

2.2. Crack Growth

[12] In the absence of stress corrosion, crack growth only commences when K_I reaches the critical value K_{IC}. Above this level, individual cracks grow rapidly at speeds approaching the Rayleigh wave velocity [*Lawn and Wilshaw*, 1975]: the crack length is thus nearly instantaneously adjusted to maintain, if possible, $K_I = K_{IC}$. Hence, equating K_I to K_{IC} provides us a relation between the crack length l and the stress state (σ_1, σ_3):

$$\sigma_1(l) = \left[K_{IC}/\sqrt{\pi a} + \sigma_3(c_3 + A_3(c_1 + c_2))\right]/[A_1(c_1 + c_2)]. \tag{14}$$

The function $\sigma_1(l)$ exhibits a maximum, denoted σ_1^{peak}, which corresponds to the short term strength of the rock in the original *Ashby and Sammis* [1990] approach. At a given imposed axial stress $\sigma_1^0 \leq \sigma_1^{\text{peak}}$, equation (14) gives the corresponding equilibrium crack length l_0. We use this procedure to determine the initial length of the cracks at the start of the brittle creep simulations with constant applied stress (σ_1, σ_3).

[13] In water-saturated environments, it is known from both experiment and theory that crack growth can occur even when $K_I < K_{IC}$. There are several empirical relationships that relate the crack growth rate dl/dt to the stress intensity factor. Laboratory tests of sub-critical crack growth of single mode I macrocracks in rocks [e.g., *Atkinson*, 1984] are in good agreement with *Charles*'s [1958] law:

$$\frac{dl}{dt} = \dot{l}_0 (K_I/K_{IC})^n, \tag{15}$$

where $\dot{l}_0$ is a characteristic crack speed, and n is an empirical exponent, commonly called the stress corrosion index, that is generally in the range 14–60 for water-saturated polycrystalline rocks [*Atkinson and Meredith*, 1987]. Other laws, relating crack growth rate to an exponential function of K_I or K_I^2 [e.g., *Wiederhorn and Bolz*, 1970; *Darot and Guéguen*, 1986], also exist and are discussed in Section 3.3.

[14] The combination of equations (10) and (15) yields an ordinary differential equation that governs the finite evolution of the wing crack length over time. Unfortunately, no analytical solution is available for this equation, and we therefore resort to numerical integration to access the solution.

2.3. Macroscopic Strain and Strain Rate

[15] Now that we have a full description of the individual crack length history, we have to relate it to the evolution of the macroscopic strain experienced by the rock. The total axial strain increment between time t and $t + dt$ is partitioned between the elastic strain and the additional irreversible strain resulting from crack growth, that we simply denote $d\epsilon_1$. This additional strain can be derived from the variation in elastic energy dW induced by crack growth, which is [*Rice*, 1968]

$$dW = N_V \frac{2\pi(l + \alpha a)}{E} K_I^2 dl, \tag{16}$$

where E is the Young's modulus of the crack free rock. Note that we neglect here the contribution of mode III stress intensity factors that act along the edges of the initial cracks during sliding: this contribution has previously been shown to decrease in importance and hence become negligible compared to the contribution of K_I as the wing cracks extend [e.g., *Kachanov*, 1982b; *Bhat et al.*, 2011].

[16] The corresponding irreversible strain increment is thus $d\epsilon_1 = (\partial dW)/(\partial \sigma_1)$, and after some algebra we obtain

$$\frac{d\epsilon_1}{dt} = \frac{3\rho_0}{(\alpha a)^3}(l + \alpha a)\frac{K_I\sqrt{\pi a}}{E}[A_1(c_1 + c_2)]\frac{dl}{dt}. \tag{17}$$

The accumulated strain $\epsilon_1(t)$ can then simply be computed numerically by integrating equation (17).

3. Results

3.1. General Features

[17] We first illustrate model predictions for the case of Westerly granite, for which all the parameter values can be independently determined from existing experimental data. The critical mode I stress intensity factor of wet Westerly granite at room temperature is K_{IC} = 1.74 MPa m$^{1/2}$ [*Atkinson and Rawlings*, 1981]. Data from triaxial deformation tests at constant strain rate obtained by *Brace et al.* [1966] provide the differential stress at the onset of cracking as a function of confining pressure. The empirical relation $\sigma_{1c} = 3.6\sigma_3 + 100$ MPa yields a reasonable linear fit to their data. The identification of this empirical relation with the theoretical relation (4) yields a friction coefficient $\mu = 0.7$, and a consequent initial flaw size of a = 1.1 mm; close to the expected *Byerlee* [1978] friction coefficient and the mean grain size of 0.8 mm for Westerly granite. As mentioned previously, in the 3D case the parameter β is used to regularize the solution for K_I at small l. We constrain its value following the procedure of *Bhat et al.* [2011], by maintaining consistency between the rigorous expression of the axial stress at the onset of opening of the wing cracks, σ_{1c} (equation (4)), and the general formulation of the axial stress at $l = 0$, $\sigma_1(l = 0)$ (equation (14)), which yields

$$\beta = \frac{1}{\pi}\frac{\sqrt{1+\mu^2} + \mu}{\sqrt{1+\mu^2} - \mu}, \tag{18}$$

i.e., β = 1.15. This value is larger than the theoretical value in 2D, equal to 0.1 [*Ashby and Sammis*, 1990], as well as the value of 0.45 chosen by *Ashby and Sammis* [1990]. Our value of β = 1.15 produces very reasonable fits to short term strength data, and the benefits of our procedure is to avoid more arbitrary choices of β and to reduce the number of fitting parameters. The initial damage parameter ρ_0 can be determined by fitting the short term failure stress for various σ_3 with the maximum stress given by relation (14). Using failure stresses of Westerly granite documented by *Mogi* [1966], a reasonable agreement is found for $\rho_0 = 2.8 \times 10^{-3}$. Finally, the parameters of the crack growth law (equation (15)) are determined from *Atkinson and Rawlings* [1981], which yields $\dot{l}_0$ = 0.24 m s^{-1} and n = 34.

[18] Using the parameters given above, we compute a simulated creep test at a confining pressure σ_3 = 30 MPa, and a differential stress $\sigma_1 - \sigma_3$ = 450 MPa, i.e., at 85% of the short term strength ($\sigma_1^{\text{peak}} - \sigma_3$ = 531 MPa). At this stress level, the initial equilibrium crack length determined from equation (14) is l_0 = 1.44 mm. Figure 3 shows normalized stress intensity factor K_I/K_{IC}, crack length l, inelastic axial strain ϵ_1 and inelastic strain rate $\dot{\epsilon}_1$, all as functions of time. Three phases can be distinguished. First, the crack growth and strain decelerate as the stress intensity factor decreases, producing a decrease in strain rate. Then, the stress intensity factor and the crack growth rate stabilize, and the strain rate remains approximately constant. Finally, the crack growth rate, and thus the strain rate, increase dramatically as the

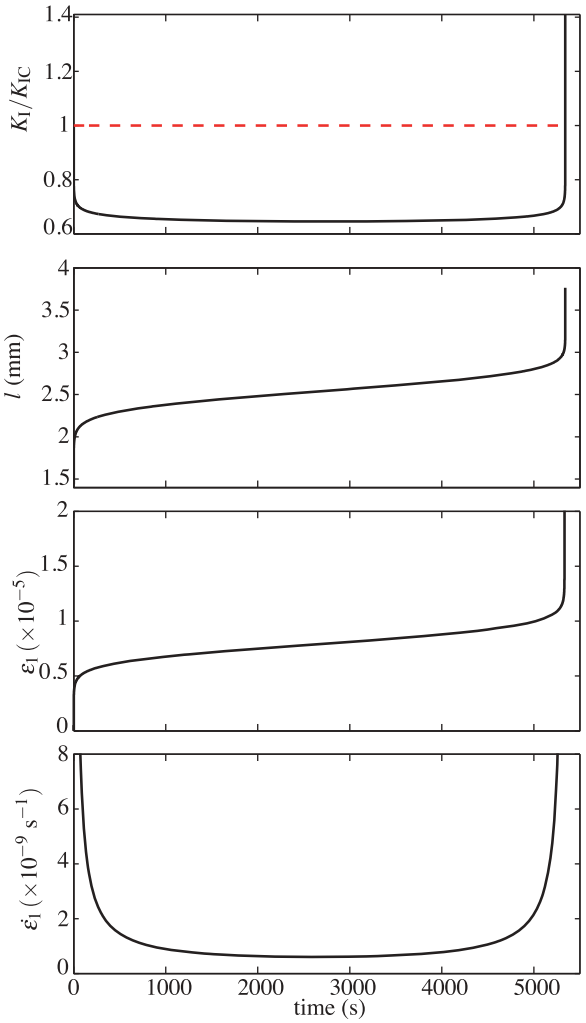

Figure 3. Evolution of the stress intensity factor, crack length, inelastic axial strain and strain rate as functions of time for a creep simulation at $\sigma_1 - \sigma_3 = 450$ MPa on Westerly granite. Other parameter values are reported in Table 1.

stress intensity factor increases and approaches K_{IC}. The three creep phases predicted by the model are remarkably similar to the commonly observed primary, secondary and tertiary creep phases in laboratory tests [e.g., *Lockner*, 1993].

[19] In the model, the primary creep phase corresponds to a decrease in K_I with increasing wing crack length. This might seem counter-intuitive, but is entirely as expected for the growth of mode I cracks under all-round compression [e.g., *Kachanov*, 1982c], as illustrated in Figure 4 (bottom, black line). In the present model, this behavior arises naturally as the loading of wing cracks is modeled by a point force, the contribution of which to K_I is proportional to $l^{-3/2}$. However, crack interactions (through the σ_3^i term in equation (8)) tend to increase the stress intensity factor, and when interactions become dominant K_I becomes an increasing function of crack length, equivalent to tertiary creep. The contribution of crack interactions to the stress intensity factor (and hence to the crack growth rate) tends to infinity when $S = \pi(l + \alpha a)^2$, i.e.,

$$l = \alpha a\left(\rho_0^{-1/3} - 1\right). \tag{19}$$

Between these two phases, K_I/K_{IC} reaches a minimum, which corresponds to the minimum rate of crack growth. It is also worth noting that the minimum in K_I/K_{IC} during sub-critical cracking at constant stress (black lines in Figure 4) occurs at the same critical crack length (l_{peak}) as the peak stress in the absence of sub-critical cracking when $K_I = K_{IC}$ (red lines in Figure 4). In this framework, secondary creep therefore appears naturally as an inflexion between primary and tertiary creep. The large value of stress corrosion index, $n = 34$, implies a large sensitivity of strain rate to K_I/K_{IC}. The low strain rates achieved when K_I/K_{IC} is at its minimum (of the order of 10^{-8} s^{-1}) explain why the system spends most of its time in the secondary creep phase, with a seemingly constant strain rate.

3.2. Derivation of an Approximate Creep Law

[20] In this section we derive a simple approximation for the minimum strain rates that characterize secondary creep in the model, so that they can be compared with the constant secondary creep strain rates measured in experiments. Since the minimum crack growth rate in the model corresponds to the minimum stress intensity factor, we first derive an expression for the minimum in K_I/K_{IC}. We observed above that the minimum in K_I/K_{IC} at constant stress occurs at the same crack length as the peak stress when $K_I = K_{IC}$. Indeed, taking the derivative of equation (8) with respect to l, we observe that for

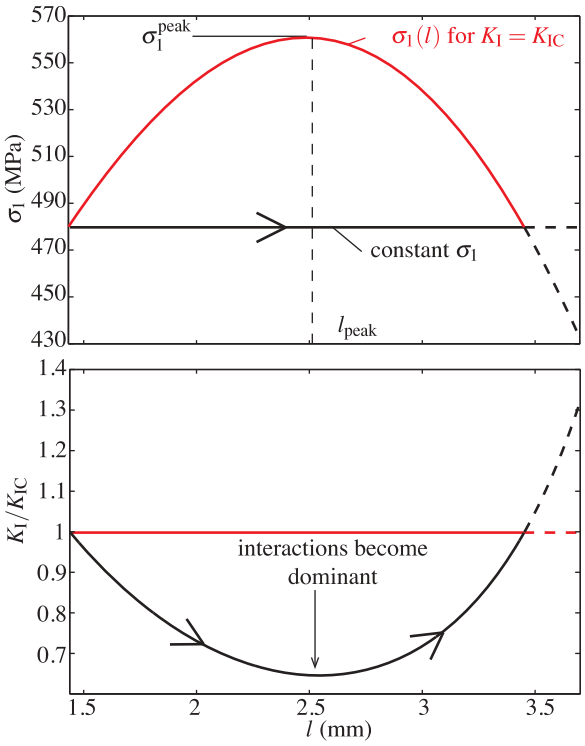

Figure 4. (top) Axial stress as a function of crack length for $K_I = K_{IC}$ (equation (14)) and for the simulated creep test at constant axial stress. (bottom) Normalized stress intensity factor as a function of crack length for the same two cases. Arrows show the sense of evolution in time.

$K_I = K_{IC}$ the crack length at peak stress ($\partial\sigma_1/\partial l = 0$) satisfies

$$\left(A_1\sigma_1^{peak} - A_3\sigma_3\right)\left(c_1' + c_2'\right) - \sigma_3 c_3' = 0, \tag{20}$$

where the prime symbol indicates differentiation with respect to l, and for constant stress σ_1, the crack length at the minimum of K_I (i.e., $\partial K_I/\partial l = 0$) satisfies

$$(A_1\sigma_1 - A_3\sigma_3)(c_1' + c_2') - \sigma_3 c_3' = 0. \tag{21}$$

For σ_1 near σ_1^{peak}, which is relevant for typical brittle creep conditions, equations (20) and (21) are very similar, and the resulting estimates of l_{peak} are quantitatively very close. For example, in the case depicted previously (for an applied differential stress equal to 85% of the peak differential stress), the relative difference between the two lengths is equal to 2.3%. Using this approximation, we can write an expression for the minimum in K_I as a function of σ_1^{peak}:

$$\min\left\{\frac{K_I}{K_{IC}}\right\} = 1 - k\frac{\sigma_1^{peak} - \sigma_1}{K_{IC}/\sqrt{\pi a}}, \tag{22}$$

where $k = A_1(c_1(l_{peak}) + c_2(l_{peak}))$ is a nondimensional numerical factor. Using $\mu = 0.7$, $l_{peak} \sim a$ and $\beta \sim 1$, we find that k is of the order of 0.1. The minimum crack growth rate is thus

$$\min\{\dot{l}\} = \dot{l}_0\left[1 - k\frac{\sigma_1^{peak} - \sigma_1}{K_{IC}/\sqrt{\pi a}}\right]^n. \tag{23}$$

[21] Considering that the strongest dependency of the strain rate is on the crack growth rate (which varies over several orders of magnitude due to the relatively high value of the stress corrosion index), the minimum strain rate in the model, corresponding to the secondary creep strain rate observed in experiments, is estimated from equations (17) and (23) as

$$\min\{\dot{\epsilon}_1\} \approx C\left[1 - k\frac{\sigma_1^{peak} - \sigma_1}{K_{IC}/\sqrt{\pi a}}\right]^{n+1}, \tag{24}$$

where C is a parameter with unit s^{-1} (i.e., a characteristic strain rate) whose order of magnitude can be estimated from

$$C \sim \dot{l}_0\frac{3\rho_0}{(\alpha a)^3}(a + \alpha a)\frac{K_{IC}\sqrt{\pi a}}{E}k, \tag{25}$$

where we took $l \sim a$ as characteristic crack length.

[22] The model also predicts a minimum stress level below which stress corrosion cracking ceases and hence tertiary creep to failure will not occur. In general, stress corrosion in single mode I cracks is only possible above a certain stress intensity level, which is generally of the order of 0.4 to 0.5 of K_{IC} [see, e.g., *Rice*, 1978; *Segall*, 1984; *Wan et al.*, 1990]. Inspection of equation (22) shows that K_I decreases below the stress corrosion threshold, denoted xK_{IC}, in finite time if $\min\{K_I/K_{IC}\} \le x$, i.e., when

$$\sigma_1 \le \sigma_1^{peak} - \frac{(1-x)K_{IC}}{k\sqrt{\pi a}}. \tag{26}$$

A lower bound of the brittle creep limit can be found by taking $x = 0$, i.e., assuming that stress corrosion acts down to $K_I = 0$. For the case of Westerly granite, a value of $x = 0.5$ can be determined from the analysis of *Segall* [1984]. At $\sigma_3 = 30$ MPa, the minimum stress is equal to 417 MPa, so that stress corrosion cracking ceases at around 77% of the peak differential stress.

3.3. Other Choices for the Crack Growth Law

[23] As mentioned previously, Charles' law is not the only existing sub-critical crack growth law. Exponential laws of the form $\dot{l} \propto \exp(bK_I)$ [*Wiederhorn and Bolz*, 1970] or $\dot{l} \propto \exp\left(bK_I^2\right)$ [*Darot and Guéguen*, 1986] have also been used, with an empirical constant b. The expression for the minimum stress intensity factor (equation (22)) can be used to determine the corresponding approximate creep laws,

$$\min\{\dot{\epsilon}_1\} \propto \exp\left[b\left(1 - k\frac{\sigma_{peak} - \sigma_1}{K_{IC}/\sqrt{\pi a}}\right)\right] \tag{27}$$

or

$$\min\{\dot{\epsilon}_1\} \propto \exp\left[b\left(1 - k\frac{\sigma_{peak} - \sigma_1}{K_{IC}/\sqrt{\pi a}}\right)^2\right]. \tag{28}$$

[24] At high stress σ_1 (i.e., for low $\sigma_{peak} - \sigma_1$), these two laws take the same asymptotic form as the power law derived previously. However, *Atkinson* [1984] noted that, in practice, most experimental data are not precise enough to discriminate between these crack growth laws.

[25] By contrast, at low stress, the deformation rates predicted by the different laws become significantly different. In this paper we use the creep law derived from Charles' law since there is an important corpus of studies that report sub-critical crack growth in terms of stress corrosion index [e.g., *Atkinson*, 1984; *Atkinson and Meredith*, 1987].

4. Application and Discussion

4.1. Comparison With Experimental Data

[26] In order to quantitatively test the parameters involved in the micromechanical brittle creep law, the model predictions are compared with experimental data obtained under triaxial conditions. We note, however, that the model is only applicable over a limited range of the experimental observations. First, since the model is based on Charles' law, it is strictly only applicable to sub-critical crack growth controlled by stress corrosion. As reported by *Anderson and Grew* [1977], above a certain rate, sub-critical crack growth is controlled by transport of reactive species to crack tips rather than by stress corrosion reactions. Second, the model approach to crack interactions, through the internal stress σ_3^i, is a simplification that becomes increasingly invalid with the increasing crack coalescence and strain localization that leads to macroscopic failure. Nevertheless, we are able to model deformation during both primary and secondary creep up to the onset of tertiary creep and acceleration to failure.

[27] Thus, we focus on the relation between the brittle creep strain rate (as observed experimentally during secondary creep) and the applied differential stress, using

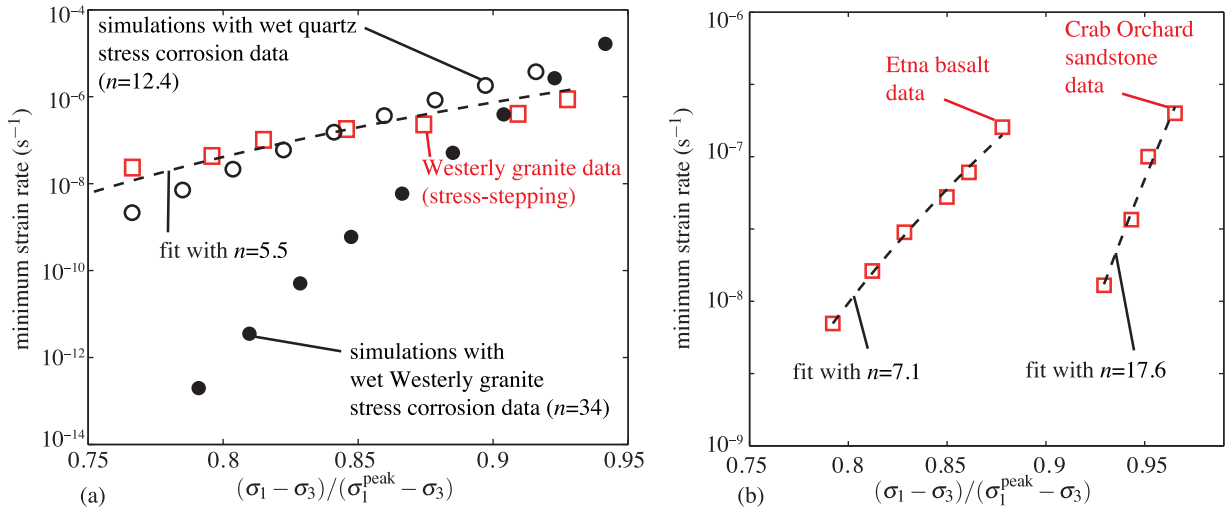

Figure 5. Comparison between model predictions and experimental data in (a) Westerly granite (this study) and (b) Etna basalt [*Heap et al.*, 2011] and Crab Orchard sandstone [*Heap et al.*, 2009b]. Data points are shown in red, predictions are in black, et the dashed lines are least squares fits to the data using equation (24).

published strain rate data from stress-stepping creep tests on low porosity (∼3.3%) Crab Orchard sandstone [*Heap et al.*, 2009b] and on Etna basalt [*Heap et al.*, 2011], and new data on Westerly granite. The selected data were collected under triaxial conditions at 50 MPa confining pressure and 20 MPa pore pressure, i.e., an effective pressure $\bar{\sigma}_3 = 30$ MPa, and at room temperature. Under these conditions, the short term strength of Crab Orchard sandstone, Etna basalt and Westerly granite are 403 MPa, 387 MPa and 530 MPa, respectively. The stress stepping method (see details in *Heap et al.* [2009a]) was used to eliminate the effect of sample variability in the determination of the brittle creep strain rates.

[28] The predicted creep strain rates as a function of normalized differential stress $(\sigma_1 - \sigma_3)/(\sigma_1^{peak} - \sigma_3)$ are given in Figure 5a for the set of parameters determined independently for Westerly granite in the previous section (filled black circles). It is clear that the model predictions do not match the experimental data (red squares in Figure 5a). In particular, the stress sensitivity predicted by the model with $n = 34$ is far too high. One possible explanation for this discrepancy is that the high stress corrosion index obtained in single crack experiments (in this particular case, from double torsion tests [*Atkinson and Rawlings*, 1981]) is valid only for cracks much larger than the grain size of the rock: in order to propagate macroscopically, the crack has to traverse numerous individual grains and grain boundaries. By contrast, for the case of the micromechanical model, the size of the individual wing cracks is of the same order of magnitude as the grain size: it is thus likely that they propagate within individual grains and/or along individual grain boundaries. In single crack experiments performed on single crystals, the stress corrosion indices are typically much lower; of the order of 10 [*Atkinson*, 1984]. We can again test the model predictions using stress corrosion data for quartz single crystals (see Table 1). In that case, we have $K_{IC} = 1$ MPa, $n = 12.4$ and we determined $\dot{l}_0 = 4.9 \times 10^{-3}$ m s^{-1} [*Atkinson*, 1979]. The corresponding initial flaw size is $a = 350$ μm (obtained from relation (4)), and other parameter values remain unchanged. These results are plotted in Figure 5a (open black circles). The prediction is much closer to the observation, but there is still a significant discrepancy. In order to determine the stress corrosion index that would be needed to match the observations, the experimental data are fitted to equation (24), with n and C as free parameters. Importantly, the value of k is fixed at the value determined from the forward modeling using $a = 1.1$ mm and $K_{IC} = 1.74$ MPa m$^{1/2}$, as before. The fit is displayed in Figure 5a by the dashed black line. The inverted stress corrosion index is $n = 5.5$, which is still significantly lower than the value observed in typical single crack tests. Such a low value might correspond to sub-critical crack growth along weak grain boundaries, or along cleavage planes in feldspar or biotite. Another possibility is that the actual value of K_{IC} is lower than 1.74 MPa m$^{1/2}$ (typically less than 1 MPa m$^{1/2}$ for quartz single crystals [*Atkinson*, 1984]), in which case the stress corrosion index required to fit the data would be closer to experimentally observed values, i.e., of the order of 10 (see the predicted curves using quartz data in Figure 5). Considering the uncertainties on the experimentally measured values of K_{IC} and stress corrosion index n, it is difficult to determine which explanation is the most plausible.

[29] A similar inversion procedure is followed to determine the stress corrosion index in Etna basalt and Crab Orchard sandstone (Figure 5b, see Table 1 for parameter values). For Etna basalt, the critical stress intensity factor is set at 2.5 MPa m$^{1/2}$, the flaw size is $a = 3$ mm, the crack density parameter is $\rho_0 = 4.8 \times 10^{-3}$ and the Young's modulus is $E = 60$ GPa. The index obtained from the fit to Etna basalt data is $n = 7.1$, which is again much lower than published values for typical basalts (from $n = 22$ to $n = 171$ [*Atkinson*, 1984]). For Crab Orchard sandstone, we use $K_{IC} = 0.45$ MPa m$^{1/2}$, the flaw size is $a = 250$ μm (approximately equal to the grain size), the crack density

Table 1. Physical Properties and Model Parameters

Parameter	Westerly Granite	Westerly Granite (Qz)[a]	Crab Orchard Sandstone	Etna Basalt
Young's modulus, E (GPa)	70	70	44	60
Friction coefficient, μ	0.7	0.7	0.7	0.7
Correction factor, β	1.15	1.15	1.15	1.15
Critical stress intensity factor,[b] K_{IC} (MPa m$^{1/2}$)	1.74	1	0.45	(2.5)
Initial flaw size,[c] a (mm)	1.1	0.35	0.25	3
Initial flaw density,[d] ρ_0, $\times 10^{-3}$	2.8	2.8	3.1	4.8
Stress corrosion index,[b] n	34	12.5	13.7	–
Stress corrosion index from fits, n	5.5	–	17.6	7.1
Ref. crack growth rate,[b] l_0 (m s^{-1})	0.24	$4.9\ 10^{-3}$	398	–
Ref. crack growth rate from fits, l_0 (m s^{-1})	$7\ 10^{-5}$	$7\ 10^{-5}$	$1.5\ 10^{-6}$	$2.5\ 10^{-4}$
Activation enthalpy, H (kJ mol^{-1})	50[e]	–	31[f]	–
Preexponential factor, A (m s^{-1})	5.710^{4}[f]	–	1[f]	–

[a]Parameters in this column are chosen assuming that wing cracks propagate through quartz grains only.
[b]From *Atkinson* [1984]. The K_{IC} value for Etna basalt is assumed to be equal to that of Preshal More basalt.
[c]Calculated from relation (4) using data from *Brace and Byerlee* [1966] (Westerly granite), *Heap et al.* [2009b] (Crab Orchard sandstone), and *Heap et al.* [2011] (Etna basalt).
[d]Estimated from fits of short term peak stress data.
[e]Estimated from Barre granite data from *Kranz et al.* [1982].
[f]Estimated from fits of *Heap et al.* [2009b] data.

parameter is $\rho_0 = 3.110^{-3}$, and the Young's modulus is $E = 44$ GPa. In this case we obtain $n = 17.6$, which is within the range of reported single crack values (from $n = 17.2$ to $n = 26.3$ [*Atkinson*, 1984]).

4.2. Effects of Sample Variability

[30] A significant issue in brittle creep experiments is the difficulty of obtaining repeatable results due to the different initial damage conditions caused by natural sample variability [e.g., *Baud and Meredith*, 1997]. In the framework of our micromechanical model, the sample variability can be seen as a variation in initial parameters such as the crack density parameter ρ_0 and the flaw size a, which are reflected as variations in the short term peak stress σ_1^{peak} (see equation (14)). We therefore simulate a series of experiments performed under exactly the same loading conditions, in order to estimate how small variations in ρ_0 and a influence the brittle creep strain rate.

[31] Figure 6 illustrates the effects of ±5% changes in a and ρ_0 on the short term strength and brittle creep strain rate in Westerly granite and Crab Orchard sandstone at an effective confining pressure of 30 MPa, using the fitted parameter values from Table 1. A ±5% variation in a induces a change in creep strain rate by a factor ≈1.1 in Westerly granite and ≈1.5 in Crab Orchard sandstone, and a change in strength of ±1% in both rocks. By contrast, a ±5% variation in ρ_0 induces a change in creep strain rate of a factor ≈1.8 in Westerly granite and a factor of ≈7 in Crab Orchard sandstone, and a change in strength of ±2.5% for both rocks. Overall, the variations in a and ρ_0 induce only minor changes in short-term strength, but significant variations in long-term creep strain rate. The strain rate changes are modest in Westerly granite, but very significant in Crab

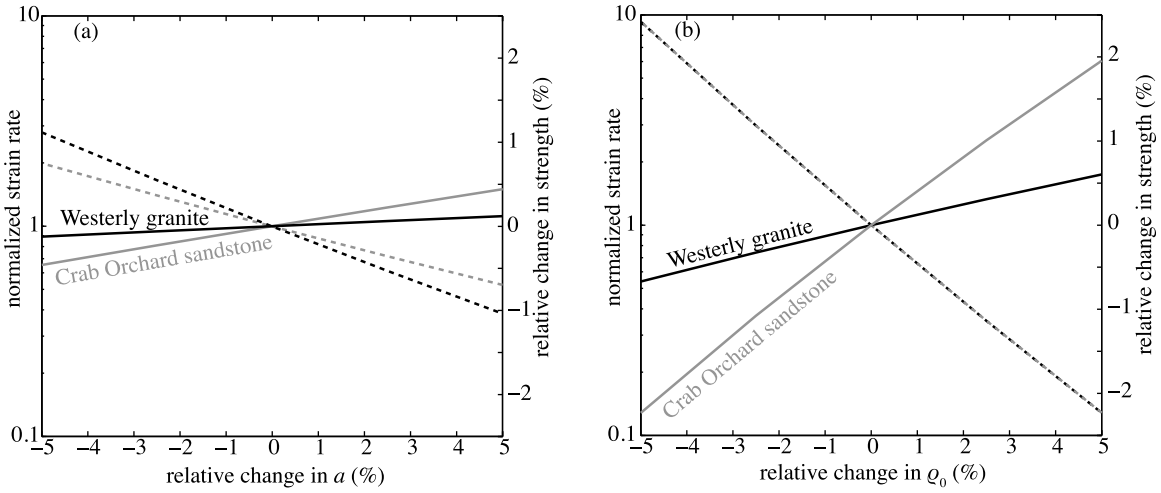

Figure 6. Effects of small variations in (a) initial flaw size a and (b) crack density parameter ρ_0 on brittle creep strain rate (solid lines) and strength (dotted lines), for Crab Orchard sandstone and Westerly granite at $\bar{\sigma}_3 = 30$ MPa. Reference parameter values are reported in Table 1. The stress corrosion index and reference crack speed are those derived from data fits. The strain rate is normalized by its value for the reference parameters set.

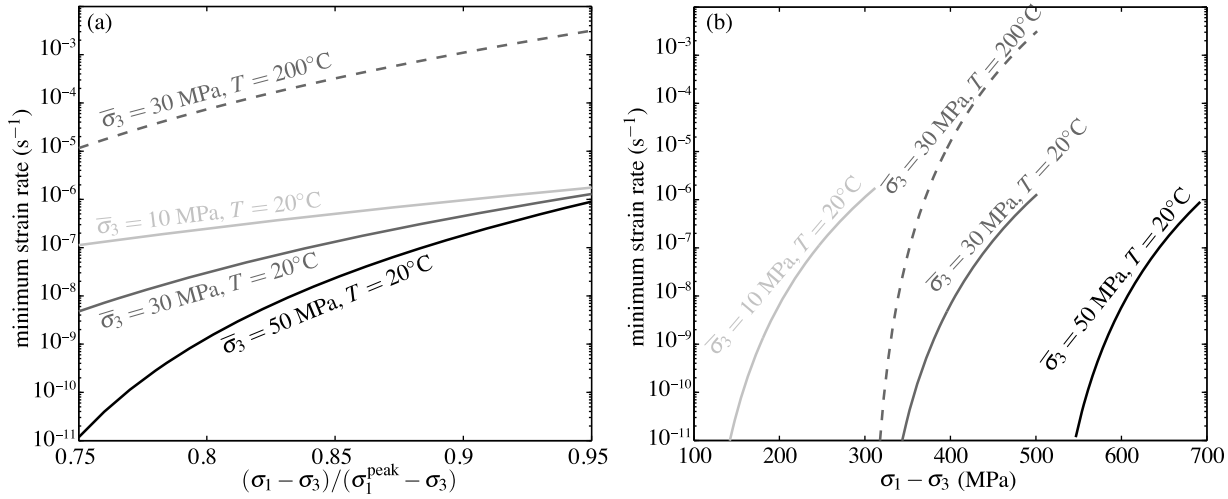

Figure 7. Brittle creep strain rate as a function of (a) normalized differential stress and (b) absolute differential stress, for Westerly granite under various effective confining pressure $\bar{\sigma}_3$ and temperature T. Parameter values are those used in section 3.1, except the stress corrosion index $n = 5.5$ and reference crack growth rate $\dot{l}_0 = 710^{-5}$ m s^{-1} which are derived from data fits. The effect of temperature is computed using relation (29) with an activation enthalpy of $H = 50$ kJ mol^{-1} [*Kranz et al.*, 1982].

Orchard sandstone. We interpret this as being due to their low ($n = 5.5$) and high ($n = 17.6$) stress corrosion indices, respectively.

4.3. Effects of Pressure and Temperature

[32] The influence of effective confining pressure ($\bar{\sigma}_3$) on creep strain rate is embedded in the model through the parameter $k = A_1(c_1(l_{peak}) + c_2(l_{peak}))$ and the peak stress σ_1^{peak}. Figure 7 shows the effects of changes in $\bar{\sigma}_3$ on the strain rate as a function of the normalized differential stress (Figure 7a) and absolute differential stress (Figure 7b). In terms of absolute differential stress, the effect of $\bar{\sigma}_3$ appears to be simple offset in strain rate. When the differential stress is normalized to the peak differential stress, there is an apparent change in stress sensitivity that arises from the dependency of strength on $\bar{\sigma}_3$.

[33] The effect of temperature can be estimated by assuming that the reference crack speed has the following form [*Atkinson*, 1984]:

$$\dot{l}_0 = Ae^{-H/RT}, \tag{29}$$

where A is a constant, H is an activation enthalpy, R is the gas constant and T is the absolute temperature. A consequence of the assumption (29) is that an increase in temperature merely offsets the strain rate, but does not change its stress dependency. It is further assumed that the strength does not change significantly with temperature. This is in general what is observed in experimental data, for example Barre granite [*Kranz et al.*, 1982] and Crab Orchard sandstone [*Heap et al.*, 2009b]. Using the activation enthalpy $H \approx 50$ kJ mol^{-1} given by *Kranz et al.* [1982] for Barre granite, we obtain the creep strain rate as a function of differential stress for various temperatures (Figure 7). In terms of absolute differential stress (Figure 7b), there is an apparent change in stress sensitivity of the strain rate which arises from the intrinsic non linearity of $\log(\dot{\epsilon}_1)$ with σ_1 (see equation (24)).

[34] In addition, it is also possible that the stress corrosion index changes with temperature [*Meredith and Atkinson*, 1982]. In that case, the sensitivity of strain rate to absolute differential stress can vary with temperature in a more complex manner, as recently illustrated for experiments on sandstones [*Heap et al.*, 2009b]. It should be noted that such a temperature dependency would arise more naturally from exponential crack growth laws, in which the parameter b that determines the stress sensitivity of the crack growth rate (see equations (27) and (28)) is of the form $b \propto 1/RT$ [e.g., *Darot and Guéguen*, 1986].

4.4. Competition Between Stress Corrosion and Pressure Solution in Porous Rocks

[35] Our micromechanical model of brittle creep is based on stress corrosion enhanced growth of wing cracks. However, in porous rocks, pressure solution is also an important time-dependent deformation mechanism [e.g., *Rutter*, 1983]. Using our simplified brittle creep law (equation (24)) with parameter values inverted from experimental data on Crab Orchard sandstone, together with models for pressure solution creep in the same rock, we can determine the range of stress and temperature conditions over which each mechanism dominates deformation.

[36] In addition to the parameters already determined in section 4.1, we also need to constrain the activation enthalpy H for stress corrosion cracking in Crab Orchard sandstone. The activation enthalpy for quartz determined from single crack tests is close to 50 kJ mol^{-1} [*Atkinson*, 1984]. However, the value estimated from triaxial brittle creep experiments [*Heap et al.*, 2009b] is closer to $H \approx 31$ kJ mol^{-1}. We therefore use the latter value in our computations.

[37] The deformation rate due to pressure solution can be calculated using the approach and parameter values from

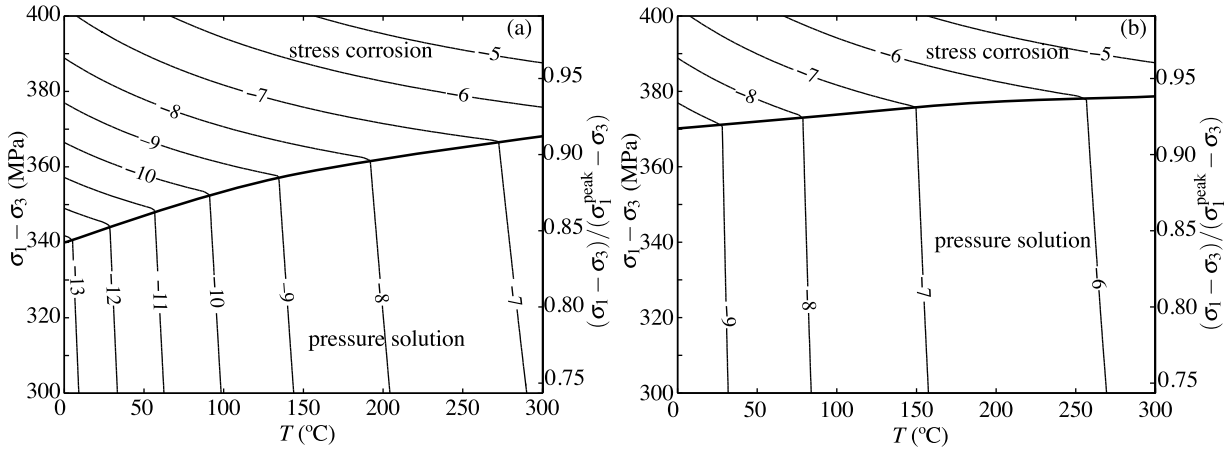

Figure 8. Deformation mechanism map of the maximum of $\log(\dot{\epsilon}_1)$ as a function of differential stress and temperature, in Crab Orchard sandstone at σ_3 = 30 MPa. Pressure solution is computed using either (a) equation (31) [from *Niemeijer et al.*, 2002] in the case of dissolution-limited rate or (b) equation (30) [from *Rutter*, 1983] in the case of diffusion-limited rate.

Rutter [1983] in the case of diffusion-limited rate, or using the model of *Niemeijer et al.* [2002] in the case of dissolution-limited rate. For the case of diffusion-limited pressure solution, the axial strain rate is given by [*Rutter*, 1983]

$$\dot{\epsilon}_1 \approx 32 A_{PS} e^{-H_{PS}/RT} \sigma_1 w / d^3, \quad (30)$$

where the preexponential factor is $A_{PS} \approx 1.05 \times 10^{-14}$, the activation enthalpy is H_{PS} = 40 kJ mol^{-1}, the width of the inter-granular fluid layer is w = 10 Å, and the grain size is d = 250 μm. For the case of dissolution-limited pressure solution, the axial strain rate can be approximated by [*Niemeijer et al.*, 2002]

$$\dot{\epsilon}_1 \approx 6\Omega \times 10^{(1.174 - 0.002028T - 4158/T)} \left[\exp\left(\frac{\sigma_1 \Omega}{RT} \right) - 1 \right] / d, \quad (31)$$

where $\Omega = 2.310^{-5}$ m^3 mol^{-1} is the molar volume of quartz. Note that equation (31) has been simplified from the more complete relation given by *Niemeijer et al.* [2002] by assuming that there is no significant stress amplification at grain contacts. Hence equation (31) provides a lower bound of the strain rate.

[38] The results are presented in the form of deformation mechanism maps for $\bar{\sigma}_3 = 30$ MPa in Figure 8. At temperatures below 50°C, the transition from stress corrosion dominated to pressure solution dominated deformation occurs at strain rates of the order of 10^{-9} s^{-1} and at differential stresses around 90% of the strength for diffusion-limited pressure solution, and at strain rates of the order of 10^{-13} s^{-1} and differential stress around 85% of the strength for dissolution limited pressure solution. At higher temperatures, stress corrosion becomes decreasingly dominant and the transition occurs at higher stress and higher strain rate. This is entirely as expected because the activation energy of stress corrosion is lower than the activation energy of pressure solution. It follows that low strain rate, long term creep due to stress corrosion is a high stress, low temperature phenomenon, relative to pressure solution creep. For other materials in which the activation energy of stress corrosion is higher than that of pressure solution, we expect that the transition from stress corrosion dominated to pressure solution dominated deformation will occur at decreasing stress with increasing temperature.

4.5. Implications for the Strength of the Crust

[39] We now use our creep law (equation (24)) to estimate the strength of the upper crust as a function of depth and strain rate. We assume a typical continental geothermal gradient of 30°C km^{-1}, a lithostatic pressure gradient of 28 MPa km^{-1} and a hydrostatic pore fluid pressure gradient of 10 MPa km^{-1}, and compute creep strain rates for Westerly granite (using parameters from fits, see Table 1) as a function of depth and differential stress (Figure 9a). Pressure solution is not expected to be an important process in this rock since the porosity is lower than 1%. Figure 9a shows that stress corrosion creep occurs only over a limited range of differential stress at any given depth, consistent with experimental observations. It is also clear that the stress sensitivity of the process increases with depth, so that the contours of strain rate become compressed with increasing depth.

[40] A similar procedure is applied to Crab Orchard sandstone, in which we expect pressure solution to also be an important time dependent deformation mechanism. In order to maintain consistency with experimental observations, we use the stress corrosion index and reference crack growth rate from the fits of triaxial creep data. The results are plotted in Figure 9b and show that stress corrosion creep occurs over an even more limited range of differential stress than for Westerly granite; again consistent with experimental observations [*Heap et al.*, 2009b]. The depth for transition from stress corrosion creep to pressure solution creep increases dramatically with increasing strain rate. For any given depth, an increase in tectonic (differential) stress will lead to a linear increase in strain rate during pressure solution. However, when the pressure solution to stress corrosion transition is reached, the strain rate will accelerate

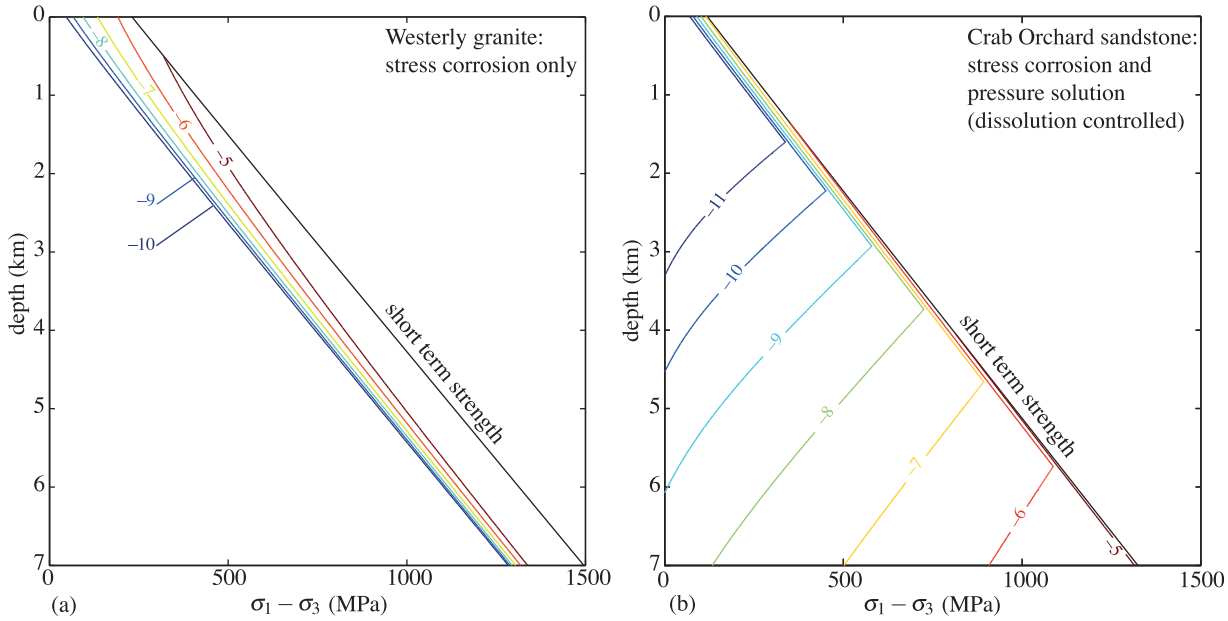

Figure 9. Contours of $\log(\dot{\epsilon})$ as a function of differential stress and depth for (a) Westerly granite and (b) Crab Orchard sandstone. The stress corrosion indices and reference crack growth rates are those derived from data fits. The strain rates for pressure solution in Crab Orchard sandstone are calculated from equation (31).

dramatically to failure, due to the much higher stress sensitivity of the stress corrosion mechanism.

[41] In all cases, we should bear in mind that brittle creep is never a steady state process. On the one hand, during pressure solution, local dissolution and precipitation processes act to decrease porosity and increase intergranular contact area, thus progressively decreasing deformation rate. We can thus speculate that, in addition to the transition from pressure solution to brittle creep as a function of pressure and temperature, there might exist a similar transition as a function of time. On the other hand, during stress corrosion creep, the damage state is continuously increasing due to subcritical crack growth, and this leads to a progressive increase in deformation rate. Hence the results shown in Figure 9 should be considered as merely snapshots of the minimum strain rate allowed for a given differential stress at a given depth. Further, once the rock has failed, the deformation process becomes frictional and our micromechanical model no longer applies without modification.

5. Conclusion

[42] We have coupled the sliding wing crack model of *Ashby and Sammis* [1990] to *Charles* [1958] description of sub-critical crack growth to explore the behavior of rocks subjected to constant differential stress in an overall compressive stress field. Our resulting model successfully reproduces the qualitative behavior observed in experiments. Primary (decelerating) creep corresponds to a decrease in the stress intensity factor at crack tips with increasing crack length, as expected for mode I cracking in compression. Tertiary (accelerating) creep corresponds to an increase in the stress intensity factor with increasing crack length due to crack interactions. Secondary creep arises as an inflexion between these two end-members.

[43] The minimum strain rate during secondary creep is well approximated by a law of the form

$$\dot{\epsilon} \propto e^{-H/RT}\left[1 - k\frac{\sigma_{\text{peak}} - \sigma_1}{K_{\text{IC}}/\sqrt{\pi a}}\right]^{n+1}, \tag{32}$$

where the stress corrosion index n gives the overall stress sensitivity. In Crab Orchard sandstone, the stress corrosion index determined from single crack experiments ($n = 13.7$) is close to that determined from fits to triaxial brittle creep strain rate data ($n = 17.6$). By contrast, the high values of n (of the order of 30 or more) determined in tensile single crack experiments in crystalline rocks such as granite and basalt, are not consistent with triaxial creep data for these rocks which yield values in the range $n = 6$ to 8. Such low values could correspond to microcrack propagation within single mineral grains or along grain boundaries.

[44] The micromechanical model can be used to estimate the strength of the upper crust as a function of creep strain rate and depth. For typical tectonic strain rates (of the order of 10^{-15} s^{-1}), the strength decreases down to the theoretical lower limit of stress that allows brittle creep $\sigma_1^{\text{peak}} - K_{\text{IC}}/(k\sqrt{\pi a})$. This corresponds to an offset in the strength that can be interpreted as a loss of cohesion. In porous rocks, creep due to stress corrosion is in competition with pressure solution creep, and we show that long term creep due to stress corrosion is a high stress, low temperature phenomenon, relative to pressure solution creep.

Appendix A: Relations Between Various Definitions of Crack Density

[45] Generally, in an isotropic matrix and for randomly oriented penny-shaped cracks, the crack density is described

by the second-order tensor γ defined by *Sayers and Kachanov* [1995] as

$$\gamma_{ij} = N_V a^3 n_i n_j, \tag{A1}$$

where **n** is a unit vector normal to the crack. In the configuration given in Figure 1, the crack density parameter ρ_0 is related to γ_{33} (vertical crack density) as

$$\rho_0 = \frac{4}{3}\pi\alpha\gamma_{33}, \tag{A2}$$

and the horizontal crack density γ_{11} is then

$$\gamma_{11} = \rho_0\left(1-\alpha^2\right)\frac{3}{4\pi\alpha^3}. \tag{A3}$$

The total (scalar) crack density, as defined by *Walsh* [1965], is $\mathrm{tr}(\gamma) = 3\rho_0/(4\pi\alpha^3)$.

[46] **Acknowledgments.** NB is grateful to Harsha Bhat, Olivier Lengliné and Chris Spiers for useful discussions and suggestions. Part of this research was funded by UK NERC grant NE/G016909/1. The authors thank the associate editor and two anonymous reviewers for their constructive comments.

References

Anderson, O. L., and P. C. Grew (1977), Stress corrosion theory of crack propagation with applications to geophysics, *Rev. Geophys.*, *15*, 77–104.

Ashby, M. F., and S. D. Hallam (1986), The failure of brittle solids containing small cracks under compressive stress states, *Acta Metall.*, *34*(3), 497–510.

Ashby, M. F., and C. G. Sammis (1990), The damage mechanics of brittle solids in compression, *Pure Appl. Geophys.*, *133*(3), 489–521.

Atkinson, B. K. (1979), A fracture mechanics study of subcritical tensile cracking of quartz in wet environments, *Pure Appl. Geophys.*, *117*, 1011–1024.

Atkinson, B. K. (1984), Subcritical crack growth in geological materials, *J. Geophys. Res.*, *89*(B6), 4077–4114.

Atkinson, B. K., and P. G. Meredith (1987), The theory of subcritical crack growth with applications to minerals and rocks, in *Fracture Mechanics of Rock*, edited by B. K. Atkinson, pp. 111–116, Academic, London.

Atkinson, B. K., and R. D. Rawlings (1981), Acoustic emission during stress corrosion cracking in rocks, in *Earthquake Prediction: An International Review*, *Maurice Ewing Ser.*, vol. 4, edited by D. W. Simpson and P. G. Richards, pp. 605–616, AGU, Washington, D. C.

Baud, P., and P. G. Meredith (1997), Damage accumulation during triaxial creep of Darley Dale sandstone from pore volumometry and acoustic emission, *Int. J. Rock Mech. Min. Sci.*, *34*(3–4), 24.e1–24.e10.

Bhat, H. S., C. G. Sammis, and A. J. Rosakis (2011), The micromechanics of Westerly granite at large compressive loads, *Pure Appl. Geophys.*, *168*(12), 1–18.

Brace, W. F., and J. D. Byerlee (1966), Stick-slip as a mechanism for earthquakes, *Science*, *153*, 990–992.

Brace, W. F., B. W. Paulding Jr., and C. Scholz (1966), Dilatancy in the fracture of crystalline rocks, *J. Geophys. Res.*, *71*(16), 3939–3953.

Byerlee, J. D. (1978), Friction of rocks, *Pure Appl. Geophys.*, *116*, 615–626.

Carter, N. L., D. A. Anderson, F. D. Hansen, and R. L. Kranz (1981), Creep and creep rupture of granitic rocks, in *Mechanical Behavior of Crustal Rocks*, *Geophys. Monogr. Ser.*, vol. 24, edited by N. L. Carter et al., pp. 61–82, AGU, Washington, D. C., doi:10.1029/GM024p0061.

Charles, R. J. (1958), Static fatigue of glass. I, *J. Appl. Phys.*, *29*(11), 1549–1553.

Costin, L. S. (1985), Damage mechanics in the post-failure regime, *Mech. Mat.*, *4*, 149–160.

Darot, M., and Y. Guéguen (1986), Slow crack growth in mineals and rocks: Theory and experiments, *Pure. Appl. Geophys.*, *124*(4–5), 677–692.

Heap, M. J., P. Baud, P. G. Meredith, A. F. Bell, and I. G. Main (2009a), Time-dependent brittle creep in Darley Dale sandstone, *J. Geophys. Res.*, *114*, B07203, doi:10.1029/2008JB006212.

Heap, M. J., P. Baud, and P. G. Meredith (2009b), Influence of temperature on brittle creep in sandstones, *Geophys. Res. Lett.*, *36*, L19305, doi:10.1029/2009GL039373.

Heap, M. J., P. Baud, P. G. Meredith, S. Vinciguerra, A. F. Bell, and I. G. Main (2011), Brittle creep in basalt and its application to time-dependent volcano deformation, *Earth Planet. Sci. Lett.*, *307*, 71–82.

Kachanov, M. L. (1982a), A microcrack model of rock inelasticity. Part I: Frictional sliding on microcracks, *Mech. Mater.*, *1*, 19–27.

Kachanov, M. L. (1982b), A microcrack model of rock inelasticity. Part II: Propagation of microcracks, *Mech. Mater.*, *1*, 29–41.

Kachanov, M. L. (1982c), A microcrack model of rock inelasticity. Part III: Time-dependent growth of microcracks, *Mech. Mater.*, *1*, 123–129.

Kemeny, J. M. (1991), A model for non-linear rock deformation under compression due to sub-critical crack growth, *Int. J. Rock. Mech. Min. Sci. Geomech. Abstr.*, *28*(6), 459–467.

Kranz, R. L. (1979), Crack growth and development during creep in Westerly granite, *Int. J. Rock Min. Mech. Sci.*, *16*, 23–35.

Kranz, R. L., W. J. Harris, and N. L. Carter (1982), Static fatigue of granite at 200°C, *Geophys. Res. Lett.*, *9*(1), 1–4.

Lawn, B. R., and T. R. Wilshaw (1975), *Fracture of Brittle Solids*, Cambridge Univ. Press, Cambridge, U. K.

Lockner, D. A. (1993), Room temperature creep in saturated granite, *J. Geophys. Res.*, *98*(B1), 475–487.

Meredith, P. G., and B. K. Atkinson (1982), High-temperature tensile crack propagation in quartz: Experimental results and application to time-dependent earthquake rupture, *Earthquake Predict. Res.*, *1*, 377–391.

Michalske, T. A., and S. W. Freiman (1982), A molecular interpretation of stress corrosion in silica, *Nature*, *295*, 511–512.

Mogi, K. (1966), Some precise measurements of fracture strength of rocks under uniform compressive stress, *Rock Mech. Eng. Geol.*, *4*, 41–55.

Nemat-Nasser, S., and H. Horii (1982), Compression-induced nonplanar crack extension with application to splitting, exfoliation, and rockburst, *J. Geophys. Res.*, *87*(B8), 6805–6821.

Niemeijer, A. R., C. J. Spiers, and B. Bos (2002), Compaction creep of quartz sand at 400–600°c: Experimental evidence for dissolution-controlled pressure solution, *Earth Planet. Sci. Lett.*, *195*, 261–275.

Paterson, M. S., and T. F. Wong (2005), *Experimental Rock Deformation—The Brittle Field*, 2nd ed., Springer, Berlin.

Rice, J. R. (1968), Mathematical analysis in the mechanics of fracture, in *Fracture: An Advanced Treatise*, *Math. Fundam.*, vol. 2, edited by H. Liebowitz, pp. 191–311, Academic, New York.

Rice, J. R. (1978), Thermodynamics of the quasi-static growth of Griffith cracks, *J. Mech. Phys. Solids*, *26*, 61–78.

Rutter, E. H. (1983), Pressure solution in nature, theory and experiment, *J. Geol. Soc.*, *140*, 725–740, doi:10.1144/gsjgs.140.5.0725.

Sayers, C., and M. Kachanov (1995), Microcrack-induced elastic wave anisotropy of brittle rocks, *J. Geophys. Res.*, *100*(B3), 4149–4156.

Scholz, C. H. (2002), *The Mechanics of Earthquake and Faulting*, 2nd ed., Cambridge Univ. Press, Cambridge, U. K.

Segall, P. (1984), Rate-dependent extensional deformation resulting from crack growth in rock, *J. Geophys. Res.*, *89*(B6), 4185–4195.

Walsh, J. B. (1965), The effect of cracks on the compressibility of rock, *J. Geophys. Res.*, *70*(2), 381–389.

Wan, K.-T., S. Lathabai, and B. R. Lawn (1990), Crack velocity functions and thresholds in brittle solids, *J. Eur. Ceram. Soc.*, *6*, 259–268.

Wiederhorn, S. M., and L. H. Bolz (1970), Stress corrosion and static fatigue of glass, *J. Am. Ceram. Soc.*, *53*(10), 543–548.

Yoshida, H., and H. Horii (1992), A micromechanics-based model for creep behavior of rock, *Appl. Mech. Rev.*, *45*(8), 294–303.